Nature Communications

https://doi.org/10.1038/s41467-026-73513-2

Article in Press

One-dimensional $CsPbBr_3$ superlattices with polarized and amplified spontaneous circularly polarized emissions

Received: 29 October 2025

Accepted: 8 May 2026

Cite this article as: Zhang, B., Chen, K., Xie, Z. *et al.* One-dimensional $CsPbBr_3$ superlattices with polarized and amplified spontaneous circularly polarized emissions. *Nat Commun* (2026). https://doi.org/10.1038/s41467-026-73513-2

Baowei Zhang, Kexin Chen, Zhengkun Xie, Kun Hu, Haiyun Dong, Yong Sheng Zhao, Liberato Manna & Siyu Lu

One-dimensional $CsPbBr_3$ superlattices with polarized and amplified spontaneous circularly polarized emissions

Baowei Zhang[1, #], Kexin Chen[1, #], Zhengkun Xie[1], Kun Hu[2,3], Haiyun Dong[2,3], Yong Sheng Zhao[2,3], Liberato Manna[4, *], Siyu Lu[1, *]

[1] College of Chemistry, Pingyuan Laboratory, Zhengzhou University, Zhengzhou, 450000, China.

[2] Beijing National Laboratory for Molecular Sciences, Institute of Chemistry, Chinese Academy of Sciences, Beijing 100190, China

[3] School of Chemical Sciences, University of Chinese Academy of Sciences, Beijing 100049, China

[4] Nanochemistry, Istituto Italiano di Tecnologia, via Morego 30, 16163 Genova, Italy.

E-mail: L. M. (*Liberato.Manna@iit.it*) and S. L. (*sylu2013@zzu.edu.cn*)

Abstract: Nanocrystal superlattices typically occur in two- or three-dimensional configurations, constrained to the micrometer scale and with limited size tunability. Here, we report one-dimensional superlattices prepared by self-assembly of $CsPbBr_3$ nanorods and nanoplatelets. These exhibit a hierarchical structure, evolving from ribbons (μm) of nanorods or nanoplatelets to assemblies of ribbons (mm). These superlattices have a diameter of 0.8-1 μm and length in the range of 13-1500 μm, and their aspect ratio can be tuned from 14 to 1200 by adjusting the shape of the nanorods and nanoplatelets. Thanks to their anisotropic structure, the superlattices show strong polarized emission with a near-unity degree of polarization, ≈4 times larger than that of randomly assembled film. These superlattices also exhibit chiral optical response (circular dichroism and circularly polarized emission). Since no chiral ligands are used in the synthesis, the chiral signal (negative or positive) from the superlattices is random. However, the signal can be controlled after the addition of chiral ligands. The maximum dissymmetry factor of the luminescence (g_{lum}) is -0.11, and can be further amplified to -0.32 in the amplified spontaneous emission of the superlattices.

Introduction

Halide perovskite nanocrystals have drawn significant attention not only because of the bright emission from individual nanocrystals,[1, 2] but also since they exhibit collective optical properties when assembled into superlattices[3-7]. For example, the electronic coupling between the constituting nanocrystals when they are organized in superlattices can induce the formation of minibands (narrow secondary energy bands arising from interparticle electronic hybridization and energy splitting) structures and result in a redshifted photoluminescence.[3, 8] Also, after interacting coherently with light, the $CsPbBr_3$ nanocrystal superlattices can emit short and intense bursts of light (so-called superfluorescence), a process that is a consequence of the long-range order of the nanocrystals in these superlattices.[4, 9, 10] The overall configuration of perovskite nano-crystal superlattices can significantly influence their collective properties.[6, 7, 11, 12] Three dimensional (3D) superlattices are the most studied cases for superfluorescence.[4, 13] Most 3D superlattices have cuboid shapes,[12, 14, 15] while a few of them are spherical,[16] rhombic-prism[11] or pyramidal.[13] Two-dimensional (2D) superlattices typically exhibit a μm-scale in the lateral direction and only a few layers of nanocrystals in the thickness direction.[6, 17-20] These 2D superlattices exhibit strongly polarized emission and thus may enhance the light outcoupling efficiency in light emitting diodes (LEDs).[6] So far, there have been only few reports on one-dimensional (1D) superlattices from perovskite nanocrystals.[21-26] It is expected that using building blocks different from cubes (the typical shape of $CsPbBr_3$ nanocrystals) may confer more structural flexibility and even chirality to the resulting 1D superlattices.[27, 28]

We report here the self-assembly of $CsPbBr_3$ nanorods (NRs) and nanoplatelets (NPLs) for the preparation of 1D superlattices having a width in the ≈0.8-1 μm range and a length in the ≈13-1500 μm range (Figure 1a). Structural analysis revealed a hierarchical organization of the superlattices: the NRs or NPLs (nm in lateral size) firstly stack into ribbons (μm in length), then the ribbons align with each other to form 1D superlattices (mm in length). The shape of the NRs/NPLs influences the aspect ratio of the superlattices, which spans the 14-1200 range. Due to their anisotropic geometry, the superlattices exhibit strong polarized emission, with a maximum degree of polarization (P) close to near unity, a value that is significantly larger than that observed from randomly assembled $CsPbBr_3$ films (Figure 1h). Also, the ribbons in the superlattices have a chiral configuration, which we ascribe to the propagation of an orientational twist of these NRs/NPLs perpendicular to their stacking direction. This configuration results in strong circular dichroism and circularly polarized emission of the 1D superlattices (Figure 1b-f). The signal (negative or positive) of the circular dichroism can be controlled by exchanging the native ligands on the surface of the NRs/NPLs with chiral ones. The maximum dissymmetry factor (g_{lum}) from these 1D superlattices is -0.11.[29-32] The chirality can be further amplified in the amplified spontaneous emission from the 1D superlattice, up to a g_{lum} of -0.32 (Figure 1d, g).

Result and discussion

Preparation of 1D superlattices from NRs/NPLs

The experimental details on the syntheses and assembly can be found in the Methods section. Briefly, $CsPbBr_3$ NRs with different diameter and length were prepared using didodecylamine (DDDAm) and oleic acid as surfactants.[33] By controlling the reaction temperature, the diameter of the NRs could be

tuned from 7.4 to 8.3 nm, while preserving an average length size of ≈40 nm, as determined by transmission electron microscopy (TEM, Supplementary Fig. 1). All the samples had pure orthorhombic $CsPbBr_3$ phase (ICSD, #97851) as seen from their X-ray diffraction patterns (XRD, Supplementary Fig. 3).[34]

After the synthesis, the NRs were dispersed in toluene (10 mg mL^{-1}) for the assembly experiments. The glass substrates were treated with perfluorodecyltriethoxysilane to enhance their interaction with the NRs solution (Supplementary Fig. 4). The NRs solution was dropped on a glass substrate positioned in the container of a Petri dish, which was then covered by the lid (Supplementary Fig. 5). During the 1-2 h evaporation time, the 1D superlattices were formed. As shown in Figure 2a-d, in this sample (named as NRs-DDDAm-1) the individual NR had a diameter of ≈8.3 nm. As seen under the optical microscope (Figure 2a), the NRs formed fibrillar-like assemblies with an average length of ≈13 μm and width of ≈0.9 μm (aspect ratio (AR) = 14, Figure 2d). Scanning electron microscopy (SEM) revealed that each fibril was comprised of clusters of ribbons (Figure 2b). Scanning transmission electron microscopy (STEM) confirmed that each individual ribbon was the result of edge-up stacking of NRs (Figure 2c).[22] This multi-scale morphology characterization thus revealed a hierarchical structure of the 1D superlattices.

The NRs-DDDAm-2 sample, consisting of NRs with a diameter of 7.8 nm, also formed 1D superlattices, this time with an average length of ≈300 μm and width of ≈0.8 μm (Figure 2e, h). These superlattices, on average, had a large aspect ratio (AR) of 375 and exhibited a "wavy" configuration (Figure 2e). SEM and TEM analyses confirmed that these superlattices as well had a hierarchical structure (Figure 2f, g). By further reducing the diameter of the NRs to 7.4 nm (Figure 2i, sample named NRs-DDDAm-3) the length of the superlattices could be increased to ≈1500 μm, with a width of ≈1.4 μm (AR=1070) (Figure 2l). Under the optical microscope (Figure 2i) also these 1D superlattices had a "wavy" configuration, and exhibited a multi-scale hierarchical structure under SEM and TEM (Figure 2j, k).

We also synthesized thin NPLs by replacing DDDAm with oleylamine (OAm) in the synthesis (Figure 2m). The NPLs in this case had a length of 35 nm and a width of 26 nm (they were named "NPLs-OAm", see Supplementary Fig. 6). The NPLs have a thickness of 4.6 nm, corresponding to 5-monolayer (5-ML) $CsPbBr_3$ NPLs. The superlattices built from this sample had a length of ≈1000 μm and width of ≈0.8 μm (Figure 2p), resulting in an AR of 1250. These results indicate that the length and aspect ratio of the 1D superlattices can be controlled by adjusting the aspect ratio of the NRs/NPLs (Supplementary Fig. 8).

The NRs/NPLs stack with each other both along their thickness direction (along the long axis of 1D superlattice) and their lateral direction (along the short axis of the 1D superlattice), as shown in Supplementary Fig. 9. We have labeled the *x*-*z* directions in Figure 2c-o to show this relation. In detail, the length of the 1D superlattices (L_{SL}) follows the formula $L_{SL} = N \cdot d$ (where N is the number of NRs/NPLs along the long axis, and d is the sum of thickness of a single NPL and the length of a partial interdigitated ligand layer). Correspondingly, the width of the 1D superlattices (W_{SL}) follows the formula $W_{SL} = M \cdot l$ (where M is the number of NRs/NPLs along the short axis, and l is the lateral size of a single NR/NPL).

For the vertical direction (along the long axis of the 1D superlattices), the inter-nanoparticle spacing (d_z) can be directly calculated based on SAXS data (Supplementary Fig. 10), by the formula $d_z = (2\pi/q) - d_0$, where $2\pi/q$ is the stacking distance measured by SAXS and d_0 is the thickness of the NPLs (or NRs). For example, the alkyl chain lengths (L) of DDDAm and OAm are ≈1.5 nm and ≈1.7 nm, respectively, and the lateral spacing (d_x) between adjacent NRs/NPLs is ≈2.3 nm and ≈3.0 nm, respectively (Supplementary Fig. 10c, d). d_z is generally smaller than twice the length of the ligands ($2L$), due to partial

interdigitation of ligands. The interdigitation factor η can be calculated as (d_z/(2L), and is usually in the 77%-80% range. Overall, the inter-nanoparticle space between adjacent NRs/NPLs increases following the increase in alkyl chain lengths of the ligands.[35, 36] The NPLs are densely stacked along the vertical direction of the 1D superlattices, but relatively loosely packed with neighboring NPLs along the lateral direction. This discrepancy arises because the lateral size distribution of the NPLs is less uniform than their thickness distribution. Ideally, the NPLs exhibit no variation in thickness. Therefore, dense packing is only achieved in the thickness direction.

To investigate the assembly process starting from the initial droplet to dried fibrillar-like assemblies, cryo-TEM analysis at different times was carried out (Figure 3). In detail, three copper net grids were placed on the substrate, and the NRs toluene solution (10 mg mL^{-1}) was drop-cast on each grid. Each grid was then rapidly plunge-frozen at different times (0, 90, 150 min) using liquid ethane. As shown in Figure 3a, the cryo-TEM images of the NRs sample at 0 min did not evidence any clear alignment globally, as the NRs mainly formed disordered clusters. At 90 min, the NRs started to organize into locally aligned zones (Figure 3b). At 150 min, globally aligned NRs were observed, in line with the corresponding 1D superlattices observed under the optical microscope (Figure 2a). Given that NPLs and NRs share a similar anisotropic nature, and considering that NPLs ultimately form even longer superlattices, we deduce that the NPLs follow a self-assembly process that is fundamentally similar to that of the NRs.

Polarized emission from the 1D superlattices

Due to their anisotropic shape, individual $CsPbBr_3$ NRs or NPLs are known to show polarized emission. [36, 37] A random assembly of NRs or NPLs on the other hand can partially average out this polarization. The ordered 1D superlattices of this work are instead built from oriented NRs or NPLs and are thus expected to preserve the polarized emission. We prepared a randomly assembled film sample (Figure 4a) and a 1D superlattice sample (Figure 4b) using NRs-DDDAm-1 as building blocks. The random film sample had a degree of polarization equal to 0.29, where $P = (I_{max} - I_{min})/ (I_{max} + I_{min})$, consistent with that of previous reports.[36, 37] In contrast, the 1D superlattices sample exhibited a P of 0.67, more than twice higher than the randomly assembled films. The other 1D superlattice samples also had high P (Figure 4c-h). The 1D NPLs-DDAB-2 superlattices sample exhibited a near unity P (0.93), the highest value for anisotropic perovskite nanocrystals to date (Figure 4i).[17, 36-45] To analyze the polarized emission direction of the samples, we employed a simplified polarization system based on a RX50M upright microscope in this study. This system consists of a polarizer and an analyzer, where the detection angle can be tuned by rotating the rotatable analyzer (0–360°). As shown in Supplementary Fig. 12, the fluorescence intensity of the sample exhibits a trend of "increase-decrease-increase-decrease" by rotating the analyzer in steps of 90°. In particular, the weakest and strongest intensity appeared at 45° and 135°, respectively, which indicates that the polarization direction is perpendicular to the long axis of the 1D superlattices, or parallel to the long axis of the NRs/NPLs. This indicates that the polarized emission stems from the building blocks of the 1D superlattices. [17, 46, 47]

Chiral optical properties of 1D superlattices

As seen in Figure 5a, the emission color of the superlattices (from blue to green) was strongly correlated with the thickness of the NRs/NPLs, and the absorption and photoluminescence spectra (Figure

5b, c) exhibited gradually blue-shifted peaks with decreasing NRs/NPLs thickness.[48] We also collected circular dichroism (CD) and circularly polarized luminescence (CPL) spectra. As seen in Figure 5d, the CD peaks of the NRs-DDDAm-1 superlattices were at 492 and 455 nm, respectively, in a mirror relation with the absorption peaks (Figure 5b). The CD spectra of the other superlattices also matched well with their absorption spectra. These rotated stacked NPLs in 1D superlattices likely exhibit distorted lattice and contribute to the chirality, similar to non-chiral ligands involved chiral $CsPbBr_3$ nanowires and nanoclusters.[29, 49] It is worth noting that the randomly assembled NPLs exhibit non-detectable CD response, while the 1D NPLs-OAm superlattices show a reasonable CD signal (g_{abs} is on the order of 10^{-3}) (Supplementary Fig. 13). This indicates that the ordered macroscopic pattern plays a key role in preserving or amplifying the intrinsic chirality.

To evaluate the thickness dependent CD spectra, we used different concentrated NPLs-OAm solutions (5-20 mg mL^{-1}) to prepare the SLs-OAm film with different thicknesses. As shown in Supplementary Fig. 16, the average thickness is determined by cross-sectional SEM. It decreases from 328 to 235 and to 145 nm, following the decrease in concentration from 20 to 10 and to 5 mg mL^{-1}. The absorption spectra and the CD spectra were collected on all the samples and the corresponding dissymmetry factors (g_{abs}) were calculated. The results indicate that the dissymmetry factor (g_{abs}) is thickness dependent: a thicker SLs film has a larger value of g_{abs} (Supplementary Fig. 16i). The CD spectra were collected using the so-called four-scan method (the sample is scanned at four different orientations, (1) $\theta = 0°$, $\beta = 0°$ (2) $\theta = 90°$, $\beta = 0°$ (3) $\theta = 0°$, $\beta = 180°$ and (4) $\theta = 90°$, $\beta = 180°$ and averages are made over the four scans) (Supplementary Fig. 17). This allowed us to subtract the contribution of linear dichroism to the CD spectra, hence retaining only the "true CD" signal.

The optical chirality was also evident in the circularly polarized emission (Figure 5e). The NPLs-DDAB-2 superlattices sample has a dissymmetry factor (g_{lum}) of -0.11 (Supplementary Fig. 20).[29, 32, 50, 51]The dissymmetry factor (g_{lum}) is $\sim 10^{-2}$, which is too small to show detectable PL intensity difference ($\approx 1\%$) in the angular resolved PL. Both the $CsPbBr_3$ NRs and NPLs can assemble into ordered 1D superlattices. As shown in Supplementary Table 1, the NPLs-based 1D superlattices exhibit larger aspect ratio, higher polarized emission and larger dissymmetry factor g_{lum} than the NRs superlattices, possibly due to the stronger anisotropic shape of the NPLs. Only the electronic ground state contributes to CD measurement, while the CPL process encompasses a broader range of excited transitions relevant for luminescence, which can lead to higher dissymmetry factors due to the cumulative effects of multiple contributing transitions[31].

Chirality control by addition of small chiral molecules

As discussed in the previous section, these 1D superlattices exhibited chiral optical response already with no involvement of chiral ligands or templates.[52, 53] We deduce that the observed chirality is attributed to the configuration of the ribbons. As shown in Figure 6a, b, the width was variable in one ribbon, although the NPLs in the starting solution were highly homogeneous in shape (Supplementary Fig. 21).This width variation suggests that each NPL is slightly rotated (twisted) along the helical axis in the ribbon compared to its neighbors (Figure 6a, b).[28, 54, 55] The rotation angle (θ) for a given NPL was calculated by the equation: $\cos\theta = L_m/L_0$, where L_m is the apparent width within the ribbon and L_0 is the actual lateral size of the NPL, taken as the maximum value of L_m observed. 3D models of the helical ribbons were then constructed based on these calculated rotation angles (Figure 6g, h). Regarding the previously reported

CdSe NPLs helices[28], these helices are well dispersed and do not interact with each other. Consequently, left- and right-handed helices are present in nearly equal amounts, resulting in a racemic system that exhibits no chiroptical response. In contrast, in our work, the densely aligned superlattices enable an autocatalytic effect[56]: an initial small fluctuation in one handedness promotes the formation of the same handedness, ultimately leading to macroscopic chiral symmetry breaking.

Statistical analysis of 50 batches of 1D NPLs-OAm superlattices revealed a near 1:1 frequency ratio between the positive and negative CD signals, confirming a near-stochastic chirality direction (Figure 6c).[31, 56] This random chirality direction was also observed in the other 1D superlattices (Figure 6d and Supplementary Fig. 22). We then introduced small chiral molecules (R/S-methylbenzylammonium bromide (R/S-MBA:Br)) during the assembly process of the NPLs. In detail, 10 mg of R-MBA: Br or S-MBA:Br dissolved in toluene were added into 3 mL of the as-obtained NPLs-OAm obtained, respectively, and the mixture was then vigorously stirred for 1 min. These NPLs were separated by adding ethyl acetate followed by centrifugation. After that, the treated NPLs were dispersed in toluene for the assembly experiments. As shown in Figure 6c, after this chiral ligand (R-MBA:Br) treatment, 50 batches of NPLs-OAm superlattices exhibited 98% (49/50) positive signals. Similarly, in the S-MBA:Br treated case, 50 batches of NPLs-OAm superlattices exhibited 100% (50/50) negative signal (Figure 6e, f). Such near unity chirality selection was also seen in the 1D NRs-DDDAm-1 superlattices (Supplementary Fig. 23). We attribute the high enantiomer-selectivity to an initial chiral distortion of the NPL lattice induced by the chiral ligands,[57, 58] which is subsequently amplified during the assembly process via an autocatalytic effect.[31, 59]

To directly investigate the stacking of NPLs in the superlattices (NPLs-OAm based 1D superlattice), we employed 3D reconstruction based on scanning TEM (Figure 6i, j). As shown in Supplementary Fig. 24, four orthoslices of stacked NPLs were collected, and used to reconstruct a 3D image (Supplementary Fig. 24a). The 3D structure is shown in Supplementary Movie 1. 3D FFT analysis of the stacked NPLs was carried out, as shown in Figure 6k, l. The discrete dots (highlighted by the gray arrows) indicate a distorted lamellar pattern between the stacked NPLs, in analogy with refs.[60, 61] These results support our hypothesis that the NPLs are stacked along their long axis with different rotation angles relative to each other. The driving force for this stacking geometry probably stems from the ligand-induced mechanical stress on $CsPbBr_3$ NPLs, which has been studied in detail for stacked CdSe NPLs.[28] Essentially, in an isolated NPL, the ligands on surface are free to rotate. However, after stacking with other NPLs, the ligands lock each other and such rotation freedom is limited.[62, 63] This translates into a reduction of the entropy and an increase of the Gibbs energy in the stacked system, generating extra mechanical stress that twists this NPL to partially recover the rotation freedom of the ligands.[28]

CP-ASE of 1D NPL superlattices

Electromagnetic simulations were performed on left-handed (LH) and right-handed (RH) one-dimensional superlattices using the COMSOL Wave Optics Module (Figure 7a-d). The experimentally measured PL spectrum was used as the incident light source, which, after modulation by the helical structure (Figure 7a, b), produced the CPL spectrum (Figure 7c). The results show that the simulated CPL characteristic peaks of the two chiral films are in strong agreement with the experimental measurements (Figure 5e), and the simulated *g*-factors were of the order of 10^{-2} (Figure 7d).

Under high-power laser pumping (35 μJ cm^{-2}) a sharp and intense emission signal was observed,

characteristic of amplified spontaneous emission (ASE), with a full width at half maximum (FWHM) of 5-7 nm (Figure 7e, f). On the other hand, the random assembled NPLs-OAm films did not show ASE under the same pumping densities (Supplementary Fig. 26). We conclude that the ordered patterns of 1D superlattices work as optical microcavities that induce ASE.[64] Optical simulations were performed to demonstrate the optical microcavities effect of 1D superlattices (Figure 7i). The results indicate that the 1D superlattices can naturally form effective Fabry–Pérot (FP) optical cavities, providing feedback for laser oscillation. This proves that the system possesses a favorable optical cavity effect.

The ASE was also circularly polarized, an effect that was ascribed to the helical configuration of the 1D superlattices. The dissymmetry factor (g) of the circularly polarized ASE was 0.26 (R) and -0.32 (S), respectively, 3-4 times higher than the g_{lum} of circularly polarized luminescence, due to enhanced coupling between the light and the chiral structures (Figure 7g, h).[65] In the microcavity, photons are confined and oscillate repeatedly. During each round trip, the right-handed circularly polarized (RCP) component experiences greater gain than the left-handed circularly polarized (LCP) component. After hundreds or thousands of round trips of amplification, the small inherent differences are continuously accumulated and amplified, leading to a rapid increase in the output g_{ASE} value, which far exceeds the intrinsic g_{lum} value. In the absence of chiral ligands or other templates, both the CPL and ASE are attributed to the twisted stacking pattern of the NPLs within 1D superlattices.[64]

This work demonstrates the fabrication, elucidation of hierarchical structure and polarized optical properties of 1D superlattices of $CsPbBr_3$ nanorod/nanoplatelets. Due to their anisotropic geometry, the superlattices show polarized emission with a near unity P value, 4 times larger than the films from the corresponding randomly assembled $CsPbBr_3$ nanorod/nanoplatelets. Also, the ribbons in the 1D superlattices have a helical configuration, resulting in strong circular dichroism and circularly polarized emission. With addition of small chiral ligands, the CD signal (negative or positive) of the superlattices can be well controlled, with an enantiomeric excess (ee) value over 98%. The maximum dissymmetry factor (g_{lum}) of the superlattice is -0.11. These 1D superlattices act as optical microcavities capable of inducing circular polarized amplified spontaneous emission, with an amplified g_{lum} factor of -0.32. This work extends the concept of 1D perovskite nanocrystal superlattices and reveals their promising properties of polarized emission, circularly polarized emission and circularly polarized amplified spontaneous emission.

Methods

Materials

Lead acetate trihydrate [$(Pb(Ac)_2 \cdot 3H_2O)$, 99.99%], cesium carbonate (Cs_2CO_3, 99%), benzoyl bromide (C_6H_5COBr, 97%), ethyl acetate (98.8%), toluene (anhydrous, 99.5%), toluene-d_8 (99 at% D), didodecyldimethylammonium bromide (DDAB, 98%), oleylamine (OAm, 70%), (R)-(+)-methylbenzylamine (R-MBA, 99%), (s)-(-)-methylbenzylamine (S-MBA, 99%), (R)-(+)-methylbenzylammonium bromide (R-MBA:Br, 99%), (S)-(-)-methylbenzylammonium bromide (S-MBA:Br, 99%), 1-octadecene (70%) and oleic acid (OA, 70%) were purchased from Sigma-Aldrich. Didodecylamine (DDDAm, 97%) was purchased from TCI. Oleylamine (70%), oleic acid (70%) and 1-octadecene (70%) were degassed at 120 °C and stored in the glovebox before use. Toluene and ethyl acetate were purchased from General Reagents Co., Ltd. and were degassed to remove residual water before use. All the other chemicals were used without any further purifications.

Synthesis of $CsPbBr_3$ nanorods (NRs-DDDAm-1)

A total of 76 mg (0.2 mmol) lead (II) acetate trihydrate, 16 mg (0.05 mmol) cesium carbonate, and 10 mL of octadecene were mixed in a 25 mL flask. The reaction mixture was degassed for 5 min at room temperature then for 1 h at 115 °C. 1.5 mL degassed oleic acid and 1.25 mmol DDDAm dispersed in 1 mL of anhydrous toluene were rapidly injected into the mixture under nitrogen. The mixture was stirred at 115 °C until all the metal salts were dissolved. The temperature was then kept at 40 °C (For NRs-DDDAm-2 and NRs-DDDAm-3, the temperature was reduced to 30 °C and 25 °C, respectively.). A total of 50 μL benzoyl bromide diluted in 500 μL of ODE was then injected into the mixture. The reaction was quenched after 15 s by immersion in a water bath (note: for NRs-DDDAm-3, an ice-water bath was used instead). Subsequently, 30 mL of an ethyl acetate and toluene mixture (with a ratio of 6:1) were added to the crude solution to precipitate the nanorods, followed by centrifugation at 6000 ×*g* for 10 min. Finally, the supernatant was discarded, and the nanorods precipitates were redispersed in toluene.

Synthesis of $CsPbBr_3$ nanoplatelets (NPLs-OAm)

A total of 76 mg (0.2 mmol) lead (II) acetate trihydrate, 16 mg (0.05 mmol) cesium carbonate, and 10 mL of octadecene were mixed in a 25 mL flask. The reaction mixture was degassed for 5 min at room temperature then for 1 h at 115 °C. 1.5 mL of degassed oleic acid and 1.25 mmol oleylamine dispersed in 1 mL anhydrous toluene were rapidly injected into the mixture under nitrogen. The mixture was stirred at 115 °C until all the metal salts were dissolved. The temperature was then lowered to 30 °C. 50 μL of benzoyl bromide diluted in 500 μL of ODE was then injected into the mixture. The reaction was quenched after 1 min by immersion in a water bath. Subsequently, 30 mL ethyl acetate/toluene mixture (with a ratio of 6:1) were added to the crude solution to precipitate the nanoplatelets, followed by centrifugation at 7000 ×*g* for 10 min. Finally, the supernatant was discarded, and the nanoplatelet precipitate was redispersed in toluene.

Ligand exchange with DDAB

All ligands exchange protocols were performed under air. Briefly, the crude reaction solution (3 mL) containing the $CsPbBr_3$ nanorods or nanoplatelets was mixed with a DDAB-toluene solution (2 mL, 25 mM) and then the mixture was vigorously stirred for 1 min. After that, the sample was precipitated by addition of 15 mL ethyl acetate, followed by centrifugation at 6000 ×*g* for 10 min. The nanorods or nanoplatelets precipitate was redispersed in a diluted DDAB-toluene solution (1 mL, 2 mM). The sample was then precipitated again following the previous protocols. The ligand exchange procedure was repeated three times to enhance the stability and emission intensity of the sample. However, excess exposure time of the nanorods or nanoplatelets to DDAB was found to cause their degradation.

Ligand exchange with R/S-MBA:Br

A solution of R/S-MBA:Br (10 mg) in toluene (2 mL) was prepared in a sample vial. The mixture was slightly heated until complete dissolution of the salt. Briefly, the R/S-MBA:Br-toluene mixture was added to crude solution of $CsPbBr_3$ nanorods or nanoplatelets (3 mL) and the resulting mixture was vigorously stirred for 1 min. After that, the sample was precipitated by addition of 20 mL ethyl acetate, followed by centrifugation at 6000 ×*g* for 10 min. The precipitate was redispersed in toluene for further assembly experiments. An excess of R/S-MBA:Br was found to cause degradation of the nanorods or nanoplatelets.

Assembly experiment

The glass slides were treated with perfluorodecyltriethoxysilane to enhance their interaction with the nanorods or nanoplatelets solution. After that, a treated glass slide was put inside the container of a Petri dish (Supplementary Fig. 4). 30 μL of the stock solution was dropped onto the glass slide by means of a

pipette. The container was then covered by the lid and then wrapped in tin foil to shield it from light and wind. With this arrangement, the solvent evaporation slowly over several hours. After that, the glass slides were recovered and used for other characterizations. If the Petri dish container was not covered by the lid, the evaporation became very fast, and the so-called 'randomly assembled film' was formed in a few minutes.

UV-Vis absorption measurements

The absorption spectra of the nanorods or nanoplatelets solutions were measured on the SHIMADZU UV-2600i UV-Vis spectrometer. The absorption spectra of the superlattices were measured on a Chirascan V100 spectrophotometer.

PL and PLQY measurements

An Edinburgh FLS1000 spectrofluorometer was employed for recording the PL of the nanorods or nanoplatelets solution and the superlattices. PLQY measurements were performed using an integrating sphere attached to the Edinburgh FLS1000 spectrofluorometer, following the absolute method.

CD and CPL measurements

The CD spectra and CPL spectra were recorded on a Chirascan V100 and JASCO CPL-300 spectrophotometers, respectively. The CD spectra were collected using the four-scan method to avoid linear dichroism and linear birefringence (LDLB) effects. The prepared sample was fixed on the test stand, and the CD signals at 0°, 90°, -0°, and -90° were measured. The average value of the four measurements was calculated as 'pure' CD signal of the sample. All data processing was performed using Origin 2021. All data are processed using the maximum-value normalization method. That is, for each spectral curve, the maximum signal intensity is set as 1, and the signal intensities of all other points on the curve are divided by this maximum value, thereby obtaining the normalized spectral data.

Polarization emission characterizations

Polarization measurements were carried out on an Edinburgh FLS980, using linearly polarized light as the excitation light source.

XRD measurements

XRD patterns were recorded on a Miniflex 600 benchtop X-ray diffractometer equipped with a 0.6 kW Cu K_a X-ray tube and a HyPix-MF 2D area detector, operating at 45 kV and 15 mA. For the measurements, the solution was deposited on a zero-background silicon wafer and the solvent was allowed to evaporate before recording the XRD patterns. The scanning angle ranged from 5° to 80° at a scan rate of 10° min^{-1}.

Amplified spontaneous emission measurements

The optically pumped lasing measurements were carried out on a far-field micro-photoluminescence measurement system equipped with a femtosecond pulsed laser (Spectra physics), an optical microscope (Nikon), a charge-coupled device camera (Nikon), and a spectrophotometer (Princeton Instruments).

SAXS measurements

The SAXS analysis was performed on a Bruker D8 Advanced X-ray Diffractometer, and the scanning 2θ angle ranged from 0.5° to 5° at a scan rate of 0.5° min^{-1}.

Optical microscopy

Optical microscopy images were collected on a SOPTOP RX50M microscope.

Transmission electron microscopy

TEM measurements were performed on a FEI Talos F200s microscope operated at 200 kV. A carbon-coated copper mesh was first placed on the glass substrate, after which a drop of the nanorods or nanoplatelets-toluene suspension was deposited on it and then evaporated to form superlattices.

Scanning electron microscopy

SEM measurements were carried out on a ZEISS Gemini 300 scanning electron microscope equipped with a SE2 secondary electronic detector operated at 3 kV. The glass slide was replaced by ITO for higher conductivity of sample.

NMR measurements

The ^{1}H-NMR tests were conducted on a Bruker-Avance NEO Ascend 500M spectrometer. The sample was dissolved in toluene-d_8 to form a high-concentrated and transparent solution.

Time-resolved Cryo-TEM analysis

Cryo-TEM was performed on a Thermo Scientific Titan Krios G3i (USA) operated at 300 kV, equipped with automatic pick-up system of frozen sample. The carbon coated copper grid was placed on the glass substrate, after which a drop of the toluene suspension containing the NCs was deposited on it and the solvent was allowed to evaporate. Following evaporation times of 0, 90, and 150 min, the sample grid was rapidly plunge-frozen using liquid ethane cooled by liquid nitrogen. Plunge-freezing was performed using a Vitrobot Mark IV (Thermo Fisher Scientific) at room temperature.

Electron tomography

Tomography series were acquired using an aberration corrected "cubed" Thermo Fisher Scientific Titan 60-300 electron microscope operated at 120 kV with a single-tilt tomography holder over a tilt range from −68° to +72°, with tilt increments of 1°. The 3D reconstruction of the tilt series was performed using the SIRT algorithm. The volume rendering, digital slicing and images were processed using Avizo.

Electromagnetic simulations

All numerical calculations were performed via finite-element simulations using the COMSOL software. Floquet periodic boundary conditions were applied in the transverse directions of the unit cell to define the wavevector, while a perfectly matched layer (PML) was adopted in the *z*-direction to simulate a reflection-free infinite domain. Simulations were carried out on structures modeled with left-handed and right-handed chirality. The incident light was directed vertically from the top port, and the left- and right-handed polarized signals modulated by the nanostructure were collected at the bottom port. Under linearly polarized light excitation, numerical simulations were performed for the left-handed and right-handed one-dimensional superlattices.

Data availability

The data that support the findings of this study are available from the corresponding authors upon request. Unprocessed raw data are provided as Supplementary Data 1. Source data are provided with this paper.

References

[1.]Protesescu L*, et al.* Nanocrystals of Cesium Lead Halide Perovskites ($CsPbX_3$, X = Cl, Br, and I): Novel Optoelectronic Materials Showing Bright Emission with Wide Color Gamut. *Nano Lett.* **15**, 3692-3696 (2015).

[2.]Li Z*, et al.* Core@Shell AgBr@$CsPbBr_3$ Nanocrystals as Precursors to Hollow Lead Halide Perovskite Nanocubes. *J. Am. Chem. Soc.* **147**, 23192-23201 (2025).

[3.]Tong Y*, et al.* Spontaneous Self-Assembly of Perovskite Nanocrystals into Electronically Coupled Supercrystals: Toward Filling the Green Gap. *Adv. Mater.* **30**, 1801117 (2018).

[4.]Rainò G, Becker MA, Bodnarchuk MI, Mahrt RF, Kovalenko MV, Stöferle T. Superfluorescence from lead halide perovskite quantum dot superlattices. *Nature* **563**, 671-675 (2018).

[5.]Zhou C*, et al.* Cooperative excitonic quantum ensemble in perovskite-assembly superlattice microcavities. *Nat. Commun.* **11**, 329 (2020).

[6.]Kumar S, Marcato T, Krumeich F, Li Y-T, Chiu Y-C, Shih C-J. Anisotropic nanocrystal superlattices overcoming intrinsic light outcoupling efficiency limit in perovskite quantum dot light-emitting diodes. *Nat. Commun.* **13**, 2106 (2022).

[7.]Filippi U*, et al.* Cooling-Induced Order–Disorder Phase Transition in $CsPbBr_3$ Nanocrystal Superlattices. *Adv. Mater.* **37**, 2410949 (2025).

[8.]Zhang J*, et al.* Thermomechanical control of electronic coupling in quantum dot solids. *J. Appl. Phys.* **107**, 123516 (2010).

[9.]Bonifacio R, Lugiato LA. Cooperative radiation processes in two-level systems: Superfluorescence. *Phys. Rev. A* **11**, 1507-1521 (1975).

[10.]Milloch A*, et al.* Halide Perovskite Artificial Solids as a New Platform to Simulate Collective Phenomena in Doped Mott Insulators. *Nano Lett.* **23**, 10617-10624 (2023).

[11.]Boehme SC*, et al.* Strongly Confined $CsPbBr_3$ Quantum Dots as Quantum Emitters and Building Blocks for Rhombic Superlattices. *ACS Nano* **17**, 2089-2100 (2023).

[12.]Gomes Ferreira M*, et al.* Self-Assembly of Quantum-Confined $CsPbBr_3$ Perovskite Nanocrystals into Rhombic, Frame, and Rectangular Superlattices. *Small Structures* **6**, 2500133 (2025).

[13.]Liu Z*, et al.* Pyramid-shaped quantum dot superlattice exhibiting tunable room-temperature coherent emission via oriented attachment. *Mater. Horiz.* **12**, 2577-2586 (2025).

[14.]Hiller JL*, et al.* Mechanically Robust Supercrystals from Antisolvent-Induced Assembly of Perovskite Nanocrystals. *ACS Nano* **19**, 26117-26126 (2025).

[15.]Baranov D*, et al.* Aging of Self-Assembled Lead Halide Perovskite Nanocrystal Superlattices: Effects on Photoluminescence and Energy Transfer. *ACS Nano* **15**, 650-664 (2021).

[16.]Tang Y*, et al.* Highly Stable Perovskite Supercrystals via Oil-in-Oil Templating. *Nano Lett.* **20**, 5997-6004 (2020).

[17.]Ye J*, et al.* Direct linearly polarized electroluminescence from perovskite nanoplatelet superlattices. *Nat. Photon.* **18**, 586-594 (2024).

[18.]Vila-Liarte D*, et al.* Templated-Assembly of $CsPbBr_3$ Perovskite Nanocrystals into 2D Photonic Supercrystals with Amplified Spontaneous Emission. *Angew. Chem. Int. Ed.* **59**, 17750-17756 (2020).

[19.]Cherniukh I*, et al.* Perovskite-type superlattices from lead halide perovskite nanocubes. *Nature* **593**, 535-542 (2021).

[20.]Cherniukh I*, et al.* Structural Diversity in Multicomponent Nanocrystal Superlattices Comprising Lead Halide Perovskite Nanocubes. *ACS Nano* **16**, 7210-7232 (2022).

[21.]Soetan N, Erwin WR, Tonigan AM, Walker DG, Bardhan R. Solvent-Assisted Self-Assembly of $CsPbBr_3$ Perovskite Nanocrystals into One-Dimensional Superlattice. *J. Phys. Chem. C* **121**, 18186-18194 (2017).

[22.]Krajewska CJ, *et al.* Controlled Assembly and Anomalous Thermal Expansion of Ultrathin Cesium Lead Bromide Nanoplatelets. *Nano Lett.* **23**, 2148-2157 (2023).

[23.]Bekenstein Y, Koscher BA, Eaton SW, Yang P, Alivisatos AP. Highly Luminescent Colloidal Nanoplates of Perovskite Cesium Lead Halide and Their Oriented Assemblies. *J. Am. Chem. Soc.* **137**, 16008-16011 (2015).

[24.]Song Y, *et al.* Efficient deep-blue LEDs based on colloidal CsPbBr3 nanoplatelets meeting the Rec.2020 standard. *Light Sci. Appl.* **14**, 336 (2025).

[25.]Dang Z, *et al.* Temperature-Driven Transformation of $CsPbBr_3$ Nanoplatelets into Mosaic Nanotiles in Solution through Self-Assembly. *Nano Lett.* **20**, 1808-1818 (2020).

[26.]Mehetor SK, Ghosh H, Pradhan N. Acid–Amine Equilibria for Formation and Long-Range Self-Organization of Ultrathin CsPbBr3 Perovskite Platelets. *J. Phys. Chem. Lett.* **10**, 1300-1305 (2019).

[27.]Zhang S, Wang X. Sub-1 nm: A Critical Feature Size in Materials Science. *Accounts of Materials Research* **3**, 1285-1298 (2022).

[28.]Jana S, de Frutos M, Davidson P, Abécassis B. Ligand-induced twisting of nanoplatelets and their self-assembly into chiral ribbons. *Sci. Adv.* **3**, e1701483.

[29.]Guha S, Bera S, Garai A, Sarma DD, Pradhan N, Acharya S. Deriving Chiroptical Properties from Intrinsically Achiral Building Blocks of One-Dimensional $CsPbBr_3$ Perovskite Nanowires. *J. Am. Chem. Soc.* **146**, 33883-33892 (2024).

[30.]Liu H, *et al.* Helical Perovskite Nanowires with Strong Circularly Polarized Luminescence Self-Assembled from Red-Emitting $CsPbI_3$ Quantum Dots Following Chiral Ligand Exchange. *ACS Nano* **19**, 17774-17784 (2025).

[31.]Zhang B, *et al.* $CsPbBr_3$ Superstructures with Circularly Polarized Photolumines-Cence Obtained by the Self-Assembly and Annealing of Nanoclusters. *Angew. Chem. Int. Ed.* **64**, e202423272 (2025).

[32.]Yao L, *et al.* Amplification of Chirality in Self-Assembled Chiral Perovskite Superstructure Films. *J. Am. Chem. Soc.* **147**, 36420-36427 (2025).

[33.]Imran M, *et al.* Shape-Pure, Nearly Monodispersed $CsPbBr_3$ Nanocubes Prepared Using Secondary Aliphatic Amines. *Nano Lett.* **18**, 7822-7831 (2018).

[34.]Hens Z, Martins JC. A Solution NMR Toolbox for Characterizing the Surface Chemistry of Colloidal Nanocrystals. *Chem. Mater.* **25**, 1211-1221 (2013).

[35.]Toso S, Baranov D, Giannini C, Manna L. Structure and Surface Passivation of Ultrathin Cesium Lead Halide Nanoplatelets Revealed by Multilayer Diffraction. *ACS Nano* **15**, 20341-20352 (2021).

[36.]Huo C, *et al.* Optical Spectroscopy of Single Colloidal $CsPbBr_3$ Perovskite Nanoplatelets. *Nano Lett.* **20**, 3673-3680 (2020).

[37.]Yang D, *et al.* Facet-induced coordination competition for highly ordered $CsPbBr_3$ nanoplatelets with strong polarized emission. *Nano Res.* **15**, 502-509 (2022).

[38.]Raja SN, *et al.* Encapsulation of Perovskite Nanocrystals into Macroscale Polymer Matrices: Enhanced Stability and Polarization. *ACS Appl. Mater. Interfaces* **8**, 35523-35533 (2016).

[39.]Güner T, *et al.* Polarized emission from $CsPbBr_3$ nanowire embedded-electrospun PU fibers. *Nanotechnology* **29**, 135202 (2018).

[40.]Zhou N, *et al.* Perovskite nanowire–block copolymer composites with digitally programmable polarization anisotropy. *Sci. Adv.* **5**, eaav8141.

[41.]Meng L, *et al.* In-situ fabricated anisotropic halide perovskite nanocrystals in polyvinylalcohol nanofibers: Shape tuning and polarized emission. *Nano Res.* **12**, 1411-1416 (2019).

[42.]He J, *et al.* In situ synthesis and macroscale alignment of $CsPbBr_3$ perovskite nanorods in a polymer matrix. *Nanoscale* **10**, 15436-15441 (2018).

[43.]Dou Y, *et al.* Lattice Distortion in Mixed-Anion Lead Halide Perovskite Nanorods Leads to their High Fluorescence Anisotropy. *ACS Materials Letters* **2**, 814-820 (2020).

[44.]Wang D, *et al.* Polarized emission from CsPbX3 perovskite quantum dots. *Nanoscale* **8**, 11565-11570 (2016).

[45.]Shi Z-F, *et al.* Polarized emission effect realized in $CH_3NH_3PbI_3$ perovskite nanocrystals. *Journal of Materials Chemistry C* **5**, 8699-8706 (2017).

[46.]Abécassis B, Tessier MD, Davidson P, Dubertret B. Self-Assembly of CdSe Nanoplatelets into Giant Micrometer-Scale Needles Emitting Polarized Light. *Nano Lett.* **14**, 710-715 (2014).

[47.]Ma X, *et al.* Anisotropic Photoluminescence from Isotropic Optical Transition Dipoles in Semiconductor Nanoplatelets. *Nano Lett.* **18**, 4647-4652 (2018).

[48.]Akkerman QA, *et al.* Solution Synthesis Approach to Colloidal Cesium Lead Halide Perovskite Nanoplatelets with Monolayer-Level Thickness Control. *J. Am. Chem. Soc.* **138**, 1010-1016 (2016).

[49.]Todd CF, Zhang JZ. Novel Chiral $CsPbBr_3$ Metal Halide Perovskite Magic-Sized Clusters and Metal Halide Molecular Clusters with Achiral Ligands. *J. Phys. Chem. Lett.* **14**, 10630-10633 (2023).

[50.]Jiang S, Kotov NA. Circular Polarized Light Emission in Chiral Inorganic Nanomaterials. *Adv. Mater.* **35**, 2108431 (2023).

[51.]Ru Y, *et al.* Full-Color Circularly Polarized Luminescence of $CsPbX_3$ Nanocrystals Triggered by Chiral Carbon Dots. *Adv. Mater.* **35**, 2207265 (2023).

[52.]Wu Y, *et al.* Ligand-Assisted Self-Assembly of 3D Perovskite Nanocrystals into Chiral Inorganic Quasi-2D Perovskites (n = 3) with Ligand-Ratio-Dependent Chirality Inversion. *Small* **19**, 2301034 (2023).

[53.]Zhang X, *et al.* Mechanically Tunable Circularly Polarized Luminescence of Liquid Crystal-Templated Chiral Perovskite Quantum Dots. *Angew. Chem. Int. Ed.* **63**, e202404202 (2024).

[54.]Zhang S, Shi W, Rong S, Li S, Zhuang J, Wang X. Chirality Evolution from Sub-1 Nanometer Nanowires to the Macroscopic Helical Structure. *J. Am. Chem. Soc.* **142**, 1375-1381 (2020).

[55.]Chen G, *et al.* Chiral All-Inorganic Perovskite Subnanowires. *J. Am. Chem. Soc.* **147**, 12347-12359 (2025).

[56.]Kondepudi DK, Kaufman RJ, Singh N. Chiral Symmetry Breaking in Sodium Chlorate Crystallization. *Science* **250**, 975-976 (1990).

[57.]Das A, Ghosal S, Marjit K, Pati SK, Patra A. Chirality of $CsPbBr_3$ Nanocrystals with Varying Dimensions in the Presence of Chiral Molecules. *J. Phys. Chem. Lett.* **15**, 7822-7831 (2024).

[58.]Wang M, *et al.* Highly Bright and Stable Chiral $CsPbBr_3$ Perovskite Nanocrystal Scintillators for High-Resolution X-ray Imaging. *Nano Lett.* **25**, 13680-13688 (2025).

[59.]Tang Y, *et al.* Electronic Coupling of Highly Ordered Perovskite Nanocrystals in Supercrystals. *ACS Appl. Energy Mater.* **5**, 5415-5422 (2022).

[60.]Xu M, Beck M, Alber F. High-throughput subtomogram alignment and classification by Fourier space constrained fast volumetric matching. *J. Struct. Biol.* **178**, 152-164 (2012).

[61.]Thompson J, *et al.* Rosalind Franklin's X-ray photo of DNA as an undergraduate optical diffraction experiment. *Am. J. Phys.* **86**, 95-104 (2018).

[62.]Yang Y, *et al.* Entropic Ligands for Nanocrystals: From Unexpected Solution Properties to Outstanding Processability. *Nano Lett.* **16**, 2133-2138 (2016).

[63.]Yang Y, Qin H, Peng X. Intramolecular Entropy and Size-Dependent Solution Properties of Nanocrystal–Ligands Complexes. *Nano Lett.* **16**, 2127-2132 (2016).

[64.]Ren S, *et al.* Circularly Polarized Lasing from Helical Superstructures of Chiral Organic Molecules. *Angew. Chem. Int. Ed.* **64**, e202415092 (2025).

[65.]Lu M, *et al.* Adaptive Helical Chirality in Supramolecular Microcrystals for Circularly Polarized Lasing. *Angew. Chem.*

Int. Ed. **63**, e202408619 (2024).

Acknowledgements

The Center of Advanced Analysis & Gene Sequencing of Zhengzhou University is thanked for Cryo-TEM testing. The authors would like to express sincere gratitude to Prof. Zhengkun Xie for his technical support in Cryo-TEM.

Funding

This work was supported by the National Natural Science Foundation of China (No. 22305224 and U24A2079), the Natural Science Foundation of Henan Province (242300421127), the China Postdoctoral Science Foundation (2022TQ0290) and the Ministry of Science and Technology of the People's Republic of China (DL2023026004L).

Author Contributions Statement

B.Z. and K.C. wrote the manuscript. K.C. prepared the figures. B.Z. and K.C. designed and directed the study. K.C. synthesized nanocrystals and conducted the structural and optical characterization experiments. Z.X. conducted the cryo-TEM experiments. K.H. assisted in the lasing experiment. H.D. and Y.S. supervised the lasing experiment. L.M. and S.L. provided suggestions on the manuscript and supervised the investigation.

Competing interests Statement

The authors declare no competing interests.

Fig. 1 | Preparation of one-dimensional superlattices exhibiting polarized emission, circularly polarized emission and amplified spontaneous emission. (a) Schematic illustration of the self-assembly of $CsPbBr_3$ NRs/NPLs into one-dimensional superlattices. (b) Circularly polarized luminescence spectra, (c) circular dichroism, and (d) amplified spontaneous emission spectra of the R-superlattices (R-SLs). (e) Circular dichroism, (f) circularly polarized luminescence spectra, and (g) amplified spontaneous emission spectra of the S-superlattices (S-SLs). (h) Polar plot of the photoluminescence intensity for 1D NPLs-DDAB-2 superlattices. All the intensities plotted in panels b-h were normalized. The red curves represent the R-SLs, while the blue curves represent the S-SLs. LPL: Linearly polarized luminescence; ASE: Amplified spontaneous emission. Fluorine-treated: The glass substrates are treated with perfluorodecyltriethoxysilane. Source data are provided as a Source Data file.

Fig. 2 | One-dimensional (1D) superlattices built by assembly of $CsPbBr_3$ NRs or NPLs of different aspect ratios. (a) Optical microscope image of the NRs-DDDAm-1 (d =8.3 nm) 1D superlattices under 365 nm light excitation. (b) SEM image of the superlattices at μm scale. (c) STEM image of the superlattices at nm scale. (d) Statistical counting of the length and width of the superlattices. (NRs-DDDAm-1: n = 100 for both width and length.) (e-h) Same characterization as in (a-d) but for the NRs-DDDAm-2 (d=7.8 nm) superlattices. (NRs-DDDAm-2: n = 100 for width, n = 30 for length.) (i-l) Same characterization as in (a-d) but for the NRs-DDDAm-3 (d =7.4 nm) superlattices. (NRs-DDDAm-3: n = 100 for width, n = 15 for length.) (m-p) Same characterization but for the NPLs-OAm (d =4.6 nm) assembled superlattices. (NPLs-OAm: n = 100 for width, n = 15 for length.) The green bars represent the width distribution, and blue bars represent the length distribution. Source data are provided as a Source Data file.

Fig. 3 | Monitoring the formation process of one-dimensional superlattices by cryo-TEM. (a-c) Cryo-TEM images during the process of solvent evaporation, for evaporation times of 0, 90, 150 min, respectively. (d) Sketches of the assembly process during the evaporation, from non-aligned to locally aligned and then to globally aligned particles.

Fig. 4 | Polarized emission from 1D superlattices. Polar plot of the photoluminescence intensity for (a) randomly assembled NRs-DDDAm-1 film and (b) 1D NRs-DDDAm-1 superlattices; (c) randomly assembled NRs-DDAB-1 film and (d) 1D NRs-DDAB-1 superlattices; (e) randomly assembled NPLs-OAm film and (f) 1D NPLs-OAm superlattices; (g) randomly assembled NPLs-DDAB-2 film and (h) 1D NPLs-DDAB-2 superlattices. (i) Degree of polarization and emission peak position from published works on anisotropic perovskite nanocrystals and our 1D NPLs-DDAB-2 superlattices. The red, yellow, purple, and cyan curves correspond to NRs-DDDAm-1/SLs-DDDAm-1, NRs-DDAB-1/SLs-DDAB-1, NPLs-OAm/SLs-OAm, and NPLs-DDAB-2/SLs-DDAB-2, respectively. Source data are provided as a Source Data file.

Fig. 5 | Chiral optical response of the 1D superlattices. (a) Optical microscope (OM) of 1D superlattices under the excitation of 365 nm light. The building blocks were NRs-DDDAm-1, NRs-DDAB-1, NPLs-OAm and NPLs-DDAB-2 from top to bottom, respectively. (b) UV-vis absorption and (c) photoluminescence spectra of NRs-DDDAm-1 (cyan), NRs-DDAB-1 (purple), NPLs-OAm (yellow) and NPLs-DDAB-2 (red) superlattices, respectively. (d) Circular dichroism and (e) circularly polarized

photoluminescence spectra of NRs-DDDAm-1 (cyan), NRs-DDAB-1 (purple), NPLs-OAm (yellow) and NPLs-DDAB-2 (red) superlattices, respectively. All the intensities plotted in panels b-e were normalized. Source data are provided as a Source Data file.

Fig. 6 | Chirality control of 1D superlattices by the addition of small chiral molecules. STEM image of (a) R-configuration ribbons and (b) S-configuration ribbons in the superlattices. Statistical counting of the CD signal for 50 batches of (c) NPLs-OAm superlattices and (d) 1D NPLs-DDAB-2 superlattices. Statistical counting of CD signal for 50 batches of (e) R-MBA:Br treated and (f) S-MBA:Br treated NPLs-OAm superlattices, respectively. The positive CD signal (red bar) was counted as +, and the negative signal (blue bar) was counted as -. The 3D model of (g) R-configuration ribbon and (h) S-configuration ribbon, respectively. The rotation angles of each NPL were calculated based on the width variation within the ribbons in STEM. (i-j) 3D reconstructed volume. The pseudocolor in panels i and j denotes the normalized contrast intensity of the 3D reconstructed volume. Bright red corresponds to regions with the maximum contrast, while dark brown indicates the minimum contrast areas. (k-l) 3D fast Fourier transform (FFT) analysis on the reconstructions of the stacked NPLs. Source data are provided as a Source Data file.

Fig. 7 | Simulated CPL response and circularly polarized ASE of the 1D superlattices. (a, b) Electric field passing through (a) right-handed chiral superlattice and (b) left-handed chiral superlattice. The color bar represents the electric field strength $|E|$, with the unit of V m^{-1}. (c) Calculated CPL response and (d) g_{lum} curve by COMSOL Wave Optics Module. The red curves represent the R-SLs, while the blue curves represent the S-SLs. (e, f) Right and left circularly polarized amplified spontaneous emission (ASE) outputs from the 1D superlattices with different chiral configurations (R-/S-), respectively. The red line represents the right-handed circularly polarized ASE component (σ^+), and the blue line represents the left-handed circularly polarized ASE component (σ^-). (g, h) Polarization angle-dependent ASE intensities from the R/S-1D superlattices, respectively. The radial axis represents the relative ASE intensity, and the angular axis represents the polarization angle. The red curves represent the R-SLs, while the blue curves represent the S-SLs. (i) Simulated field intensity distribution (λ=466 nm, n=2.6) in a superlattice with L=1.7 μm. The simulated field intensity distribution indicates that the superlattice can function as a FP optical cavity for realizing laser oscillations. The color bar represents the electric field strength $|E|$, with the unit of V m^{-1}. Source data are provided as a Source Data file.

Nanocrystal superlattices typically occur in two- and three-dimensional configurations, constrained to the micrometer scale and with limited size tunability. Here, the authors assemble $CsPbBr_3$ nanoplatelets into chiroptically active 1D helical superlattices with mm lengths and μm widths.

Peer Review Information: *Nature Communications* thanks the anonymous reviewers for their contribution to the peer review of this work. A peer review file is available.

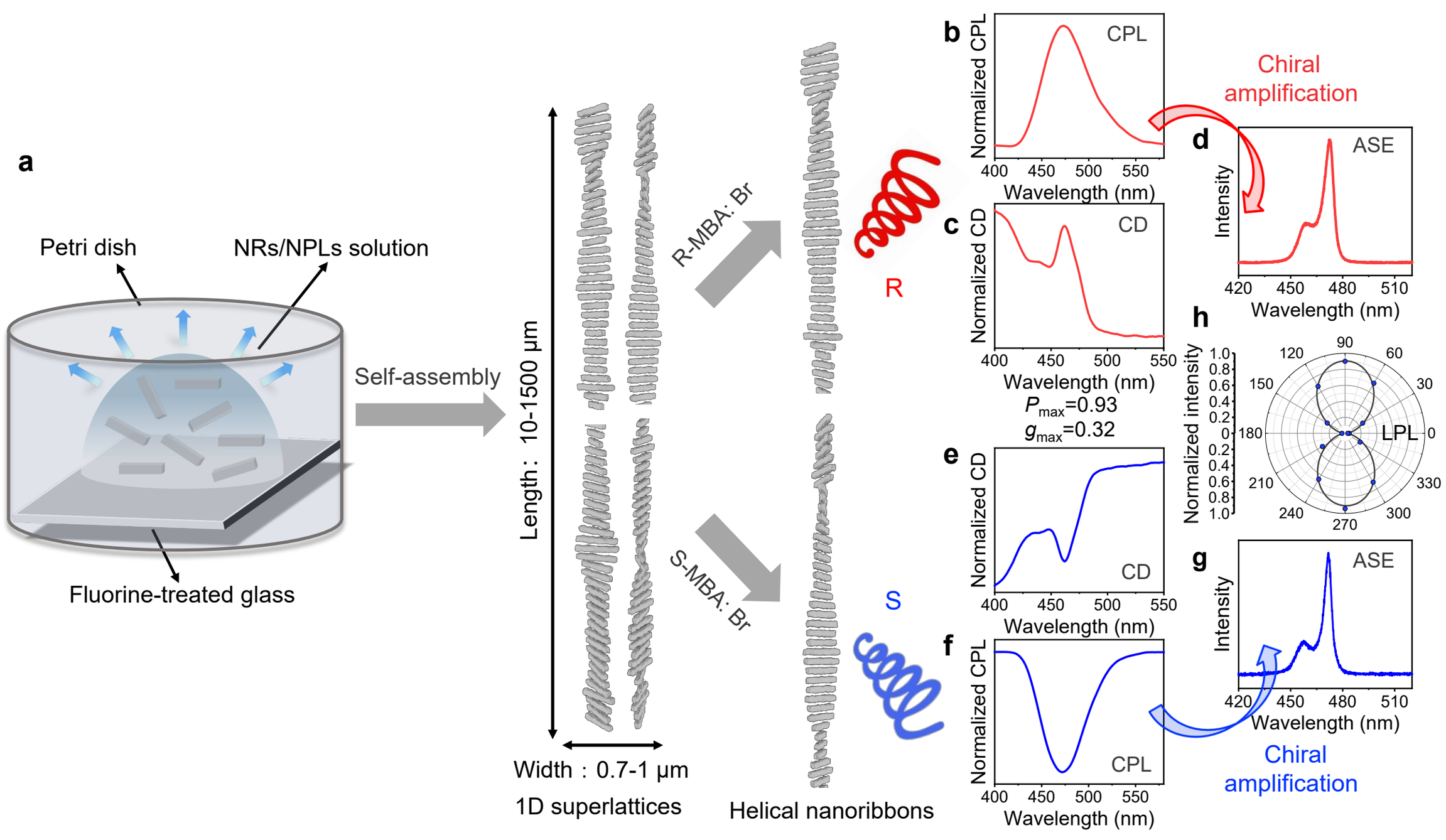
a
Petri dish
NRs/NPLs solution
Fluorine-treated glass
Self-assembly
Length: 10-1500 μm
Width : 0.7-1 μm
1D superlattices
R-MBA: Br
S-MBA: Br
R
S
Helical nanoribbons
b
CPL
Normalized CPL
Wavelength (nm)
c
CD
Normalized CD
Wavelength (nm)
P_{max}=0.93
g_{max}=0.32
Chiral amplification
d
ASE
Intensity
Wavelength (nm)
e
CD
Normalized CD
Wavelength (nm)
f
CPL
Normalized CPL
Wavelength (nm)
g
ASE
Intensity
Wavelength (nm)
Chiral amplification
h
LPL
Normalized intensity

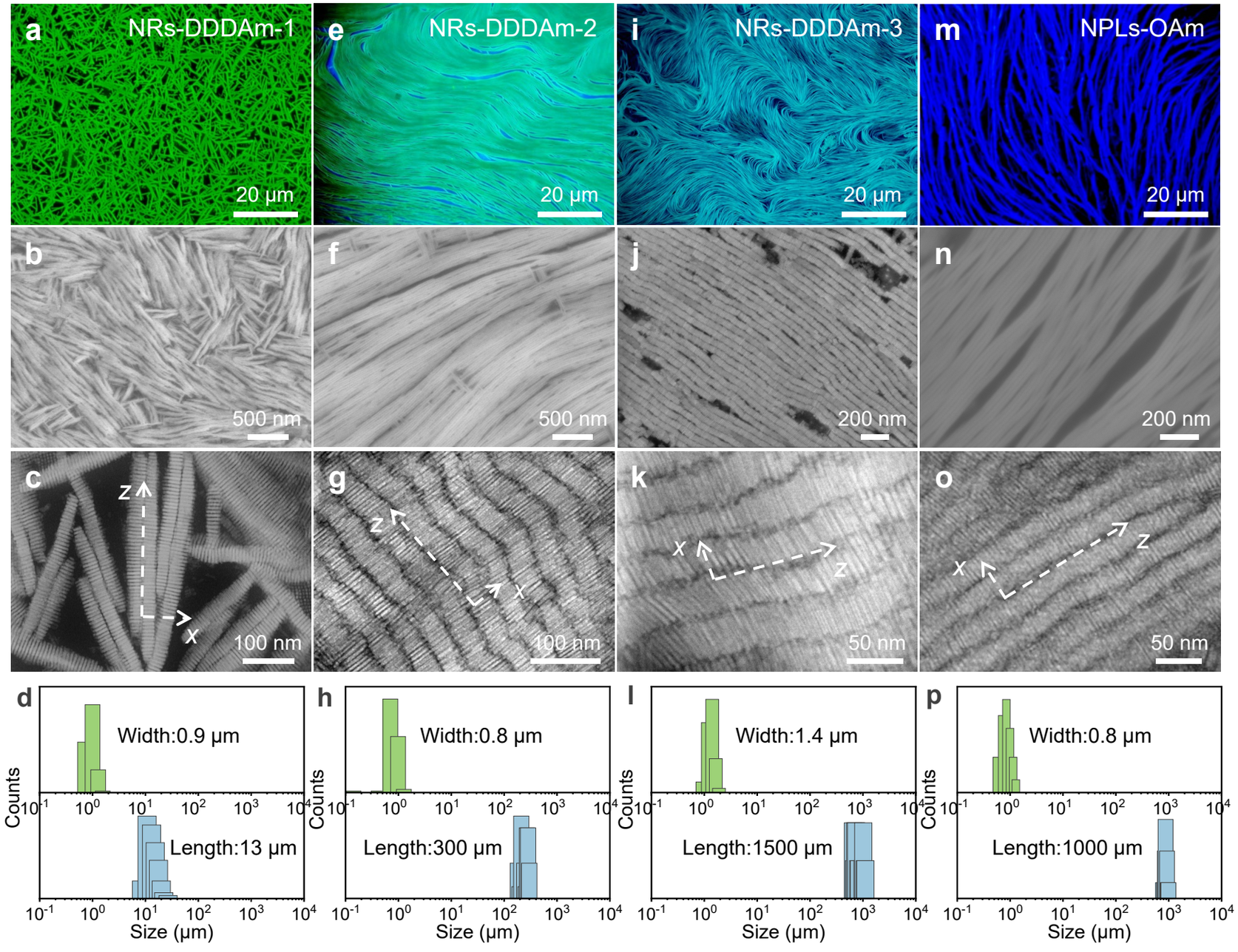
a
NRs-DDDAm-1
20 μm
e
NRs-DDDAm-2
20 μm
i
NRs-DDDAm-3
20 μm
m
NPLs-OAm
20 μm
b
500 nm
f
500 nm
j
200 nm
n
200 nm
c
z
x
100 nm
g
z
x
100 nm
k
x
z
50 nm
o
x
z
50 nm
d
Width:0.9 μm
Length:13 μm
Counts
Size (μm)
h
Width:0.8 μm
Length:300 μm
Counts
Size (μm)
l
Width:1.4 μm
Length:1500 μm
Counts
Size (μm)
p
Width:0.8 μm
Length:1000 μm
Counts
Size (μm)

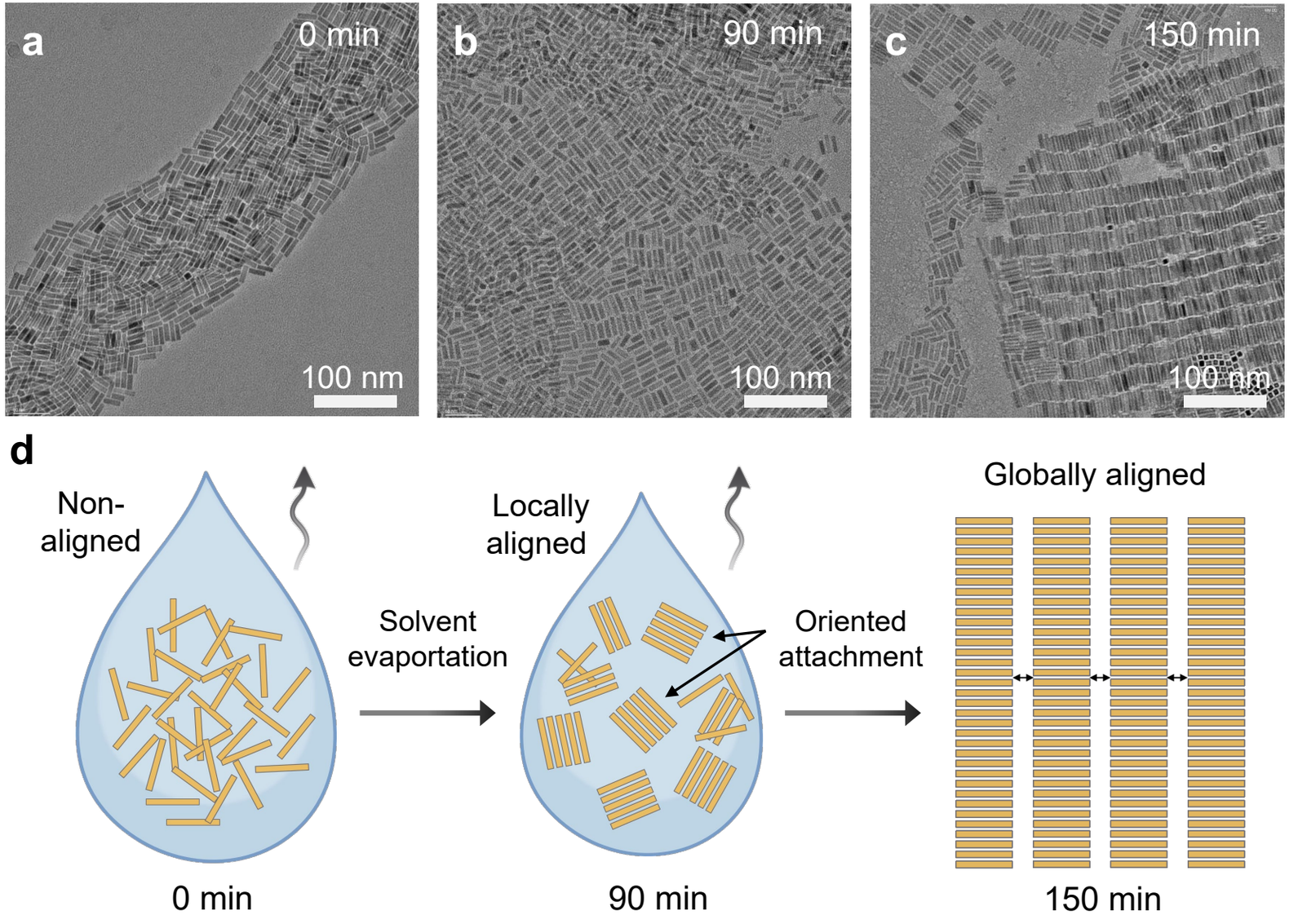
a
0 min
100 nm
b
90 min
100 nm
c
150 min
100 nm
d
Non-
aligned
Solvent
evaportation
Locally
aligned
Oriented
attachment
Globally aligned
0 min
90 min
150 min

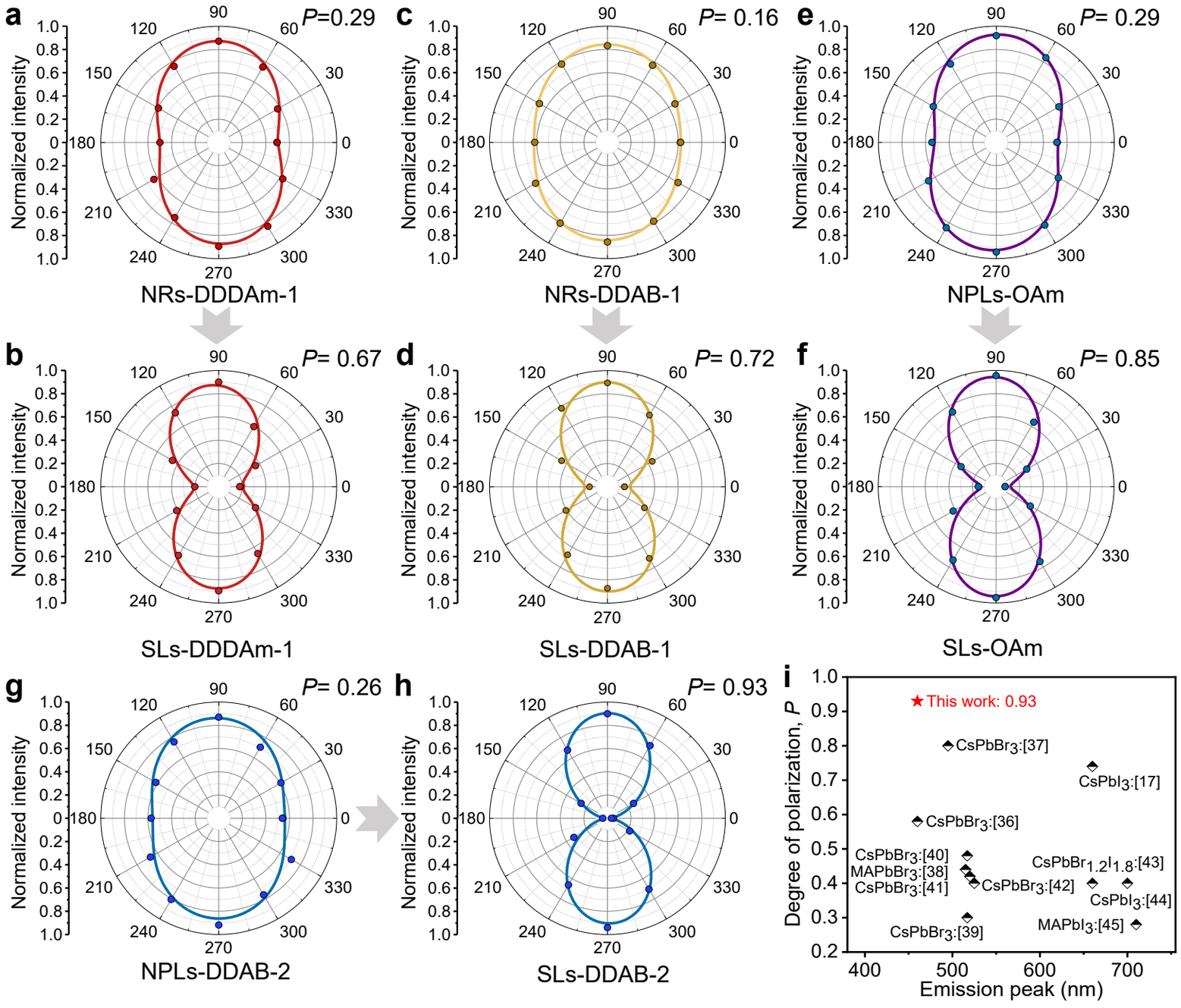
a
P=0.29
NRs-DDDAm-1
b
P= 0.67
SLs-DDDAm-1
c
P= 0.16
NRs-DDAB-1
d
P= 0.72
SLs-DDAB-1
e
P= 0.29
NPLs-OAm
f
P= 0.85
SLs-OAm
g
P= 0.26
NPLs-DDAB-2
h
P= 0.93
SLs-DDAB-2
Normalized intensity
i
★This work: 0.93
CsPbBr3:[37]
CsPbI3:[17]
CsPbBr3:[36]
CsPbBr3:[40]
MAPbBr3:[38]
CsPbBr3:[41]
CsPbBr3:[42]
CsPbBr1.2I1.8:[43]
CsPbI3:[44]
MAPbI3:[45]
CsPbBr3:[39]
Degree of polarization, P
Emission peak (nm)

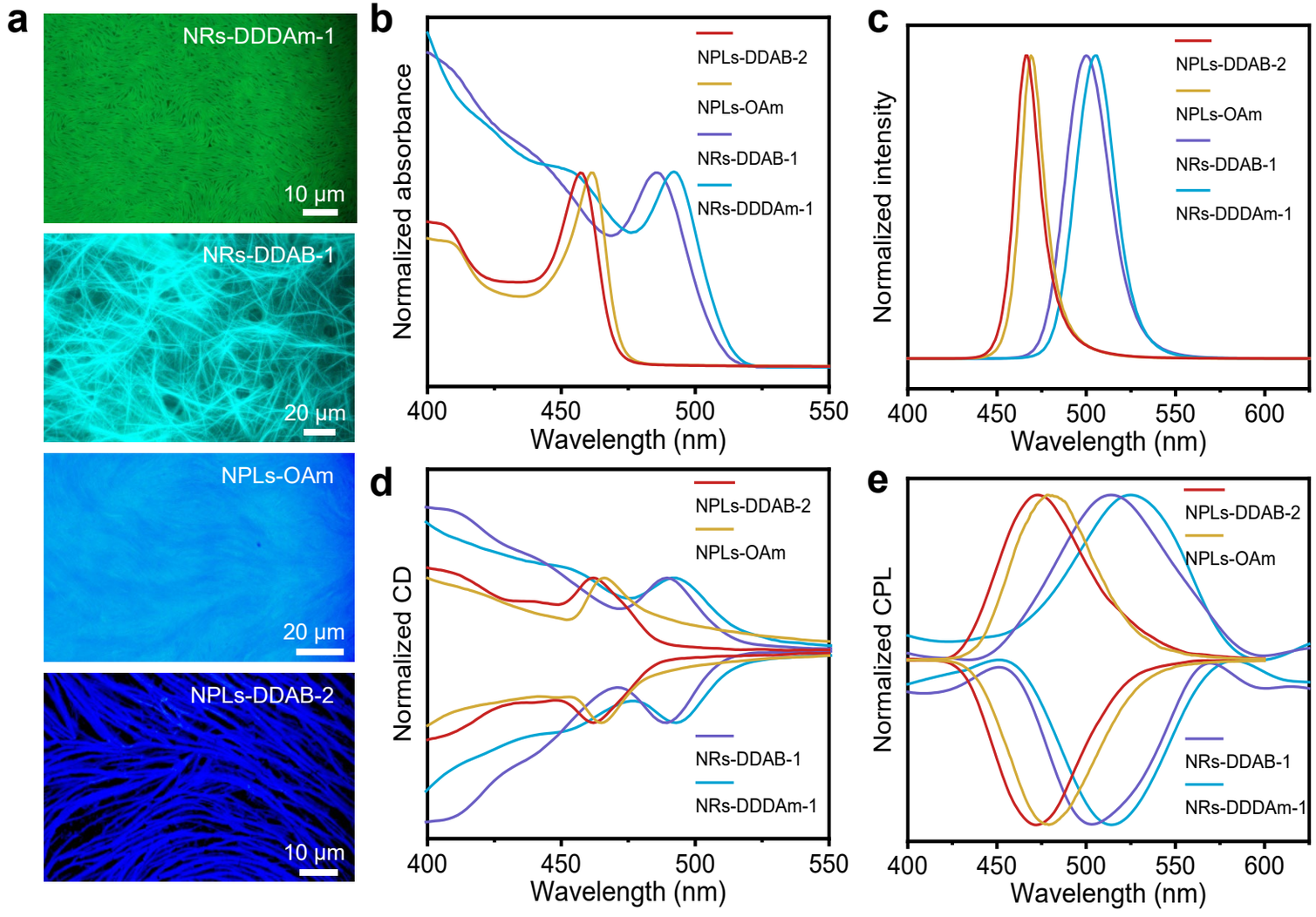
a
NRs-DDDAm-1
10 μm
NRs-DDAB-1
20 μm
NPLs-OAm
20 μm
NPLs-DDAB-2
10 μm
b
Normalized absorbance
NPLs-DDAB-2
NPLs-OAm
NRs-DDAB-1
NRs-DDDAm-1
400
450
500
550
Wavelength (nm)
c
Normalized intensity
NPLs-DDAB-2
NPLs-OAm
NRs-DDAB-1
NRs-DDDAm-1
400
450
500
550
600
Wavelength (nm)
d
Normalized CD
NPLs-DDAB-2
NPLs-OAm
NRs-DDAB-1
NRs-DDDAm-1
400
450
500
550
Wavelength (nm)
e
Normalized CPL
NPLs-DDAB-2
NPLs-OAm
NRs-DDAB-1
NRs-DDDAm-1
400
450
500
550
600
Wavelength (nm)

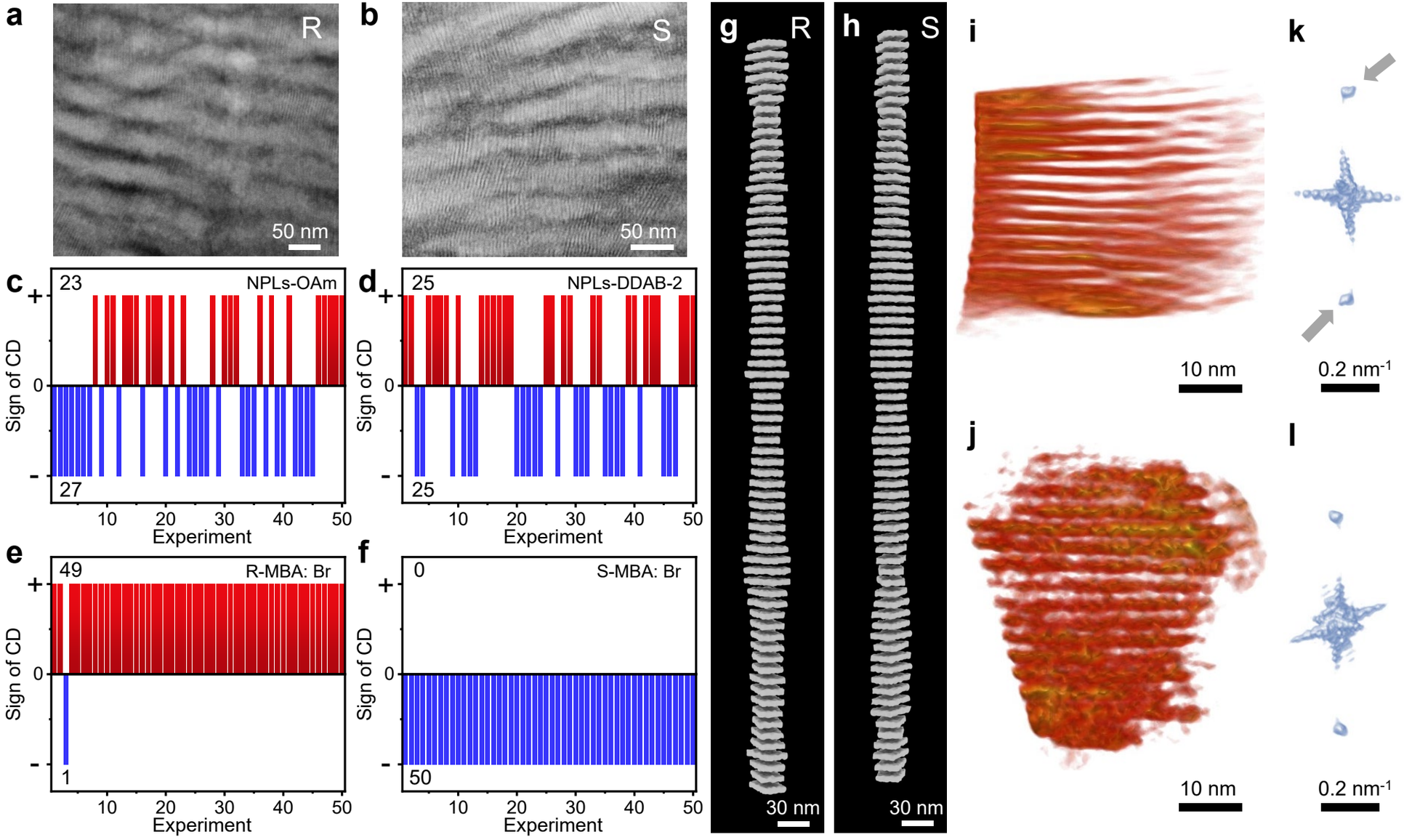
a
R
50 nm
b
S
50 nm
c
23
NPLs-OAm
+
0
-
27
Sign of CD
10 20 30 40 50
Experiment
d
25
NPLs-DDAB-2
+
0
-
25
Sign of CD
10 20 30 40 50
Experiment
e
49
R-MBA: Br
+
0
-
1
Sign of CD
10 20 30 40 50
Experiment
f
0
S-MBA: Br
+
0
-
50
Sign of CD
10 20 30 40 50
Experiment
g
R
30 nm
h
S
30 nm
i
10 nm
k
0.2 nm-1
j
10 nm
l
0.2 nm-1

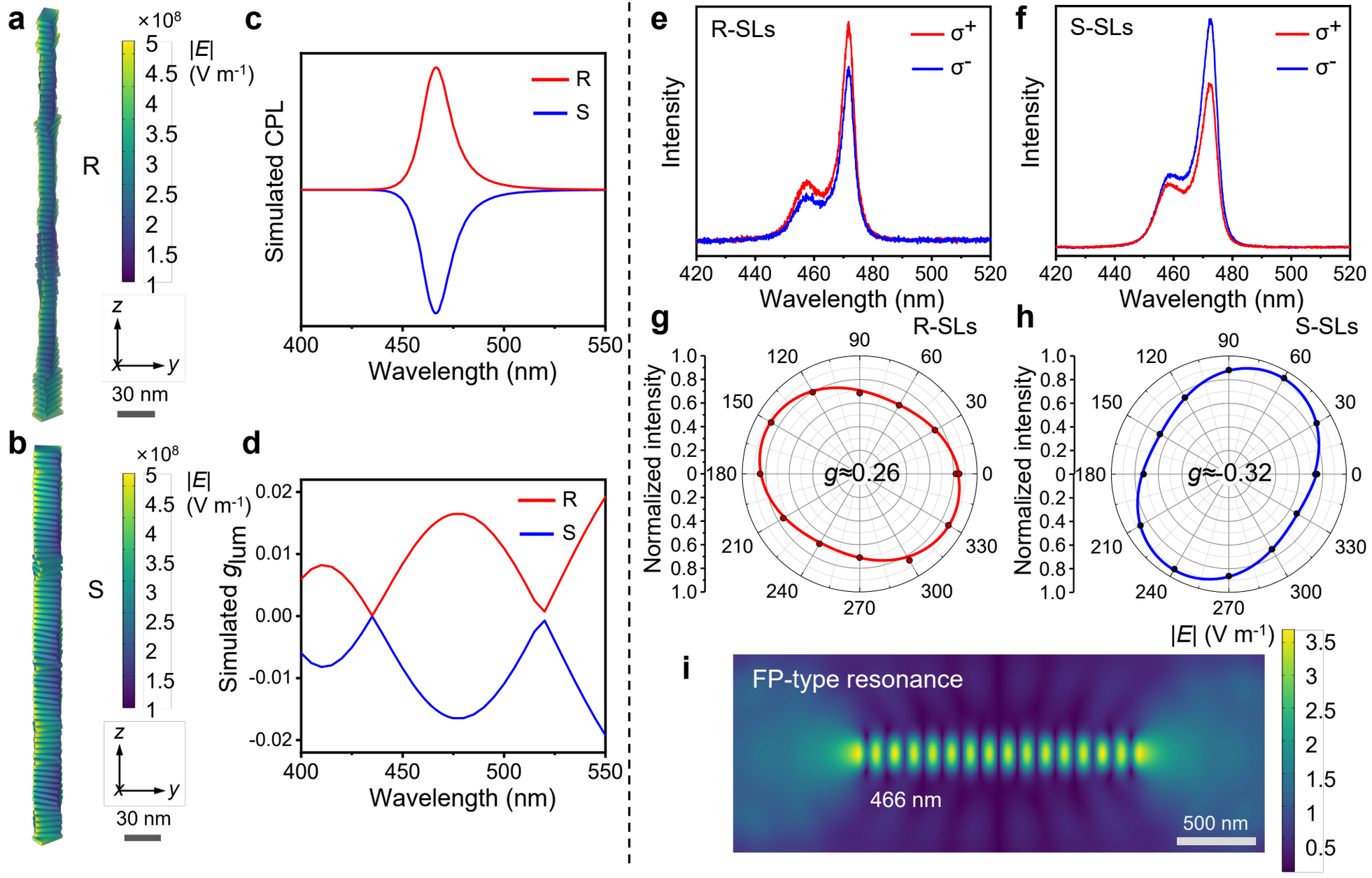
a
R
×10^8
5
4.5
4
3.5
3
2.5
2
1.5
1
|E| (V m-1)
z
y
30 nm
b
S
×10^8
5
4.5
4
3.5
3
2.5
2
1.5
1
|E| (V m-1)
z
y
30 nm
c
Simulated CPL
R
S
400
450
500
550
Wavelength (nm)
d
Simulated glum
0.02
0.01
0.00
-0.01
-0.02
R
S
400
450
500
550
Wavelength (nm)
e
R-SLs
σ+
σ-
Intensity
420
440
460
480
500
520
Wavelength (nm)
f
S-SLs
σ+
σ-
Intensity
420
440
460
480
500
520
Wavelength (nm)
g
R-SLs
Normalized intensity
1.0
0.8
0.6
0.4
0.2
0
90
120
60
150
30
180
0
210
330
240
300
270
g≈0.26
h
S-SLs
Normalized intensity
1.0
0.8
0.6
0.4
0.2
0
90
120
60
150
30
180
0
210
330
240
300
270
g≈-0.32
i
FP-type resonance
466 nm
500 nm
|E| (V m-1)
3.5
3
2.5
2
1.5
1
0.5